PHYSICAL REVIEW B **97**, 245422 (2018)

Dispersion characteristics of face modes in ionic-crystal and plasmonic-metal nanoparticles

Sean M. Collins*
Department of Materials Science and Metallurgy, University of Cambridge, 27 Charles Babbage Road, Cambridge CB3 0FS, United Kingdom

(Received 30 April 2018; revised manuscript received 12 June 2018; published 25 June 2018)

Shape-dependent modes dominate the optical states of nanoparticles in the infrared spectra of ionic crystals and in the visible spectra of plasmonic metals. Here, the characteristic dispersion, or the shift in energy associated with the spatial period of surface charge oscillations, of surface modes governed by charges on the faces of prismatic nanoparticles is shown to follow the same form as the dispersion of the antisymmetric and cavity modes of infinite thin films and cylinders. Examination of the quasistatic eigenmodes of cubic particles with and without an internal octahedral cavity reveals the origins of this antisymmetric character and demonstrates self-coupling in the particles containing cavities. In these particles, interactions between the face and cavity modes give rise to distinctive optical states at energies approaching the longitudinal optical phonon frequency in ionic crystals or the bulk plasma frequency in metal nanoparticles.

DOI: 10.1103/PhysRevB.97.245422

I. INTRODUCTION

The use of modes to describe the electromagnetic response of nanoparticles is pervasive in the application of dielectric theory to ionic crystals at infrared frequencies and plasmonic-metal particles at near infrared, visible, and ultraviolet frequencies. Modes arise for analytical solutions for high-symmetry particles [1–3], and for particles where the dimensions are significantly smaller than the corresponding wavelength, electrostatic approximations allow for a description strictly in terms of geometric eigenmodes of the particle defined in terms of surface charges [4–6]. With the development of techniques capable of directly imaging signatures of these modes, including electron-energy-loss spectroscopy (EELS) [7,8], cathodoluminescence (CL) [9,10], and near-field optical techniques [11], a complete understanding of the variety of shape-dependent particle modes is essential in nano-optics. While the dispersion of modes arising from symmetries associated with the corners and edges of prismatic nanoparticles has been described in detail, modes on the faces of prismatic particles have been reported experimentally [12–15] with little comment.

Here, the character of such face modes is explained in the context of antisymmetric thin-film surface modes and cavity modes of extended and finite systems. These systems, which exhibit the same fundamental type of dispersion characteristics as face modes in nanoparticles, are then combined to exploit these properties for tailoring the photonic states close to the longitudinal-optical (LO) phonon frequency ω_{LO} or the bulk plasma frequency ω_P in ionic-crystal and metal nanoparticles, respectively.

Since the resurgence of EELS mapping in plasmonics [7], the so-called dispersion of particles such as plasmonic rods has been examined [16–18] and likewise has been examined for ionic-crystal rods [19] once more with the introduction of EELS characterization of ionic crystal modes at meV resolution [8]. In particle dielectric theory, the term dispersion signifies the shift in mode energy as a function of $q = \omega/v$, where v is the velocity of the incident electromagnetic field and ω is the angular frequency and is associated with a wave-vector-like quantity $(2\pi/\lambda)$ determined from the spatial nodes or antinodes in the standing wave on a particle surface. In addition to rod geometries, which have been shown to follow the dispersion characteristics of infinite cylinders, the edge modes of lithography-fabricated planar rectangular structures have likewise been reported to follow a similar quasiuniversal dispersion relationship [20]. In the case of decahedral nanoparticles, the dependence of the mode energy on mode order (scaling with wave vector) has also been described in terms of tight-binding models for charges at particle corners and edges [15]. In all of these systems, as the order (defined generally in terms of the changes in sign of surface charges associated with these modes and therefore associated with the wave vector) increases, the energy of the mode increases. Notably, the energies of these modes increase toward a cluster point at the energy corresponding to the surface plasmon for a dielectric half-space ω_S, understandable given that at large wave vectors and rapid oscillations of the associated surface charge the geometry of the system has minimal effect and the modes resemble those of a planar surface (see also Refs. [2,3,5]).

This general dispersion relationship, in conjunction with the strongest optical effects often associated with low-order particle dipole modes, has promulgated a widespread description of particle optics in terms of the lowest-energy modes. In the development of surface plasmon tomography, both in approaches to the reconstruction of quasistatic eigenmodes [21] and in the reconstruction of the photonic density of states [22,23], the n lowest-energy modes have been selected for basis sets used for three-dimensional reconstructions. Similar approaches using the n lowest-energy modes have been used for the demonstration of the effect of bi-orthogonality of the eigenvectors associated with the surface charges in such systems [24].

---

*smc204@cam.ac.uk

©2018 American Physical Society

However, it has been well known since early work on the infrared response of ionic crystal cubes that some high-energy modes, specifically modes *above* the surface mode energy ω_S, contribute significantly to the optical spectrum [25,26]. These modes are described here as "face" modes based on the distribution of surface charges across the faces of prismatic nanoparticles as well as the previous descriptions of these modes observed in EELS experiments on cubes and other prismatic particles [13–15]. These modes are not captured in approaches truncating the description to the n lowest-energy modes. This work offers a description of why face modes appear at energies above ω_S, first by examining the geometric analogs in the modal description to antisymmetric thin-film surface modes and cylindrical cavity modes as well as by examining the eigenmodes of prismatic and spherical particles. In turn, these characteristics lead to a model particle geometry consisting of a cube containing an octahedral cavity which highlights possibilities for coupling face and corner modes. This geometry demonstrates unique optical properties, including pinning mode energies at the LO phonon or bulk plasma frequency, and showcases opportunities for localized creation and depletion of photonic states on nanoparticle faces.

The incorporation of cavity mode resonances is particularly relevant given recent reports of plasmonic properties in Al voids [27] as well as frame particle geometries [28,29]. The complementarity between cavity and particle modes has been understood for some time [30], but the coupling mechanisms in single-frame particles requires understanding the dispersion characteristics of particle face modes. Such coupling mechanisms will, in turn, also inform work on nanopore optics [31,32] which exhibit geometric attributes of convex and concave surfaces.

II. THEORETICAL CONTEXT FOR FACE MODE DISPERSION

In order to describe dispersion in face modes for prismatic nanoparticles, the dielectric theory formalism is briefly reviewed for high-symmetry and arbitrary-geometry cases and then used to explain the properties of two fundamental branches in surface mode energies. The origins of mode dispersion are then discussed in terms of the boundary element method (BEM) [4,5,33] before examples are presented in a series of prismatic particles with octahedral symmetry.

A. Dispersion in thin films and cylinders

Analytical solutions are possible for the modes of infinite thin films, infinite cylinders, and spheres. The symmetric modes of a film of thickness a are given by [5]

$$\varepsilon^{+}(\omega) = -\frac{1+e^{-2qa}}{1-e^{-2qa}}, \tag{1}$$

where $q = \omega/v$. The antisymmetric modes are given by replacing ε with ε^{-1}.

For a Drude dielectric function of the form $\varepsilon(\omega) = 1 - (\omega_P^2/\omega^2)$, this returns the usual expression for symmetric and antisymmetric thin-film surface plasmons [5]:

$$\omega^{\pm} = \omega_P\sqrt{\frac{1 \mp e^{-2qa}}{2}}. \tag{2}$$

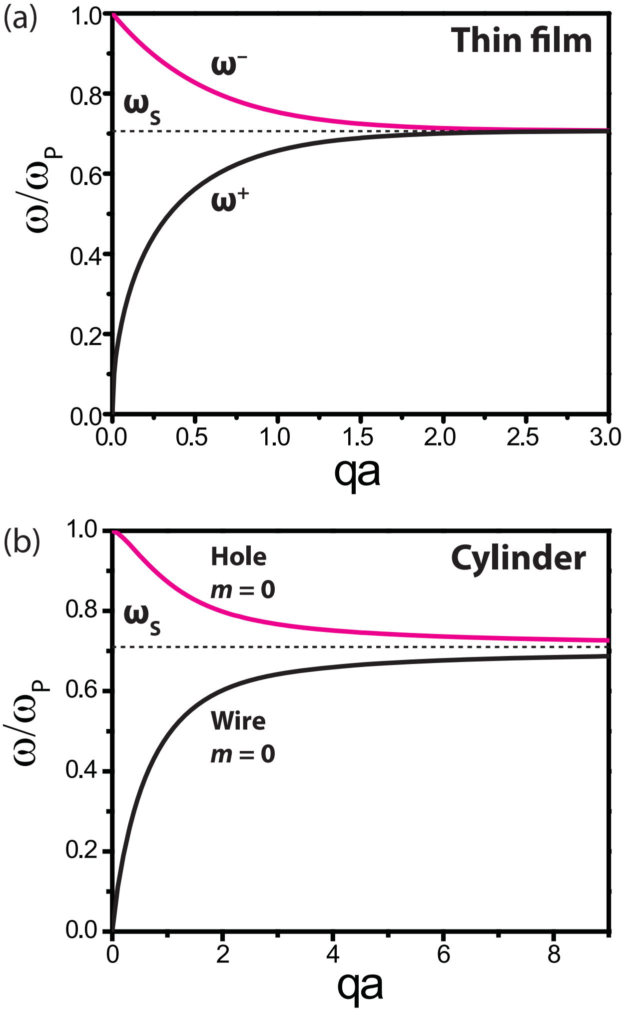

FIG. 1. Surface mode dispersion relations for (a) a thin film and (b) a cylinder. The antisymmetric (ω^-) and symmetric (ω^+) modes of the film are shaded magenta and black, respectively. The lowest-azimuthal-order ($m = 0$) modes of an infinite cylindrical hole (magenta) or wire (black) are likewise shaded according to their energy relative to the surface mode ω_S (dashed line). Mode energies are shown for a Drude dielectric function defined by bulk plasma frequency ω_P. The dispersion is plotted as a function of qa, where $q = \omega/v$ and a is the film thickness in (a) and radius in (b).

For an infinite cylinder, the modes are analogously given by [5]

$$\varepsilon_m(\omega) = \frac{I_m(qa)K_m'(qa)}{I_m'(qa)K_m(qa)}, \tag{3}$$

where again $q = \omega/v$, a is the radius of the cylinder, and I and K are the modified Bessel functions of the first and second kinds, respectively. The primes denote derivatives with respect to the arguments of the modified Bessel functions, and m gives the azimuthal symmetry [5,34]. The dispersion relation for a cylindrical hole or cavity is given, as for the antisymmetric thin-film modes, with ε replaced by ε^{-1} [5].

These dispersion relations, cast in terms of plasmonic metal structures with a Drude dielectric function, are presented in Fig. 1. The expressions in terms of ε, however, are also appropriate for surface phonon modes in ionic crystals [8,19]. In Fig. 1, it should be noted that for the thin film [Fig. 1(a)], the two branches observed are for a single structure, while the two branches for cylindrical symmetry derive from two separate structures, the convex cylindrical wire and the concave cylindrical hole [Fig. 1(b)].

In the case of finite particle modes, a sphere provides sufficient symmetry for analytical modal expansions [2,5]. In the quasistatic approximation, sphere modes are given by

$$\varepsilon_\ell = -\frac{1+\ell}{\ell}, \tag{4}$$

where the integer ℓ defines the number of nodes in the surface charge distribution.

For arbitrary particle geometries, the BEM approach in the quasistatic approximation allows for the statement of the solution of the Poisson equation as an eigenvalue problem given in terms of the surface charges σ [19]:

$$F|\sigma\rangle = \lambda_i|\sigma\rangle, \tag{5}$$

where λ_i are the eigenvalues. In alternative form, this may be written as

$$\Lambda(\omega)\sigma(\omega) = \int d\mathbf{s}' F\sigma(\mathbf{s},\omega), \tag{6}$$

where

$$F = \frac{-\mathbf{n}\cdot(\mathbf{s}-\mathbf{s}')}{|\mathbf{s}-\mathbf{s}'|^3}. \tag{7}$$

F is the normal derivative of the Coulomb kernel given in terms of $\mathbf{n}$, the surface normals for a surface element at $\mathbf{s}$ and another element at $\mathbf{s}'$. $\Lambda(\omega)$ is then defined as

$$\Lambda(\omega) = 2\pi\frac{1+\varepsilon_{\text{particle}}/\varepsilon_{\text{medium}}}{1-\varepsilon_{\text{particle}}/\varepsilon_{\text{medium}}}. \tag{8}$$

For ambient vacuum ($\varepsilon_{\text{medium}} = 1$), this expression can be further simplified in terms of the particle dielectric function only. $\Lambda(\omega)$ can now be used to relate the surface charge distribution and the dielectric function of the particle. The frequency-dependent dielectric function $\varepsilon(\omega)$ determines the eigenfrequencies ω_i for a particular eigenmode i for a given value of the dielectric function ε_i:

$$\varepsilon_i = -\frac{1+\gamma_i}{1-\gamma_i}, \tag{9}$$

where now $\gamma_i = -\lambda_i/2\pi$, following Eq. (8).

The form of these expressions is identical for ε in Eqs. (1), (4), and (9). For the thin-film modes $\gamma_i = e^{-2qa}$, and for the sphere modes $\gamma_i = (2\ell+1)^{-1}$. In each case [and also for Eq. (3)] there are two fundamental mode varieties, defined by the exchange of ε and ε^{-1}. The exchange of ε and ε^{-1} is, in fact, an exchange of $\varepsilon_{\text{particle}}$ and $\varepsilon_{\text{medium}}$ following the simplification in Eq. (8). This exchange suggests an exchange of the interior and exterior dielectric contributions to the mode, most apparent in the wire/hole geometry but also present in the thin-film and particle geometries for modes on the upper branch. The exchange of $\varepsilon_{\text{particle}}$ and $\varepsilon_{\text{medium}}$ in particle modes reflects the change in the dominant fields inside or outside the particle (see below).

The universal symmetry of the two branches is often omitted from descriptions of surface mode dispersion [19,34]. This result is linked to Apell's sum rules for complementary structures [30], although here the general case for a single particle is emphasized. Note that in the general case [Eq. (9)] these two categories are exchanged for $\lambda_i > 0$ and $\lambda_i < 0$. It can therefore be understood that, for particle eigenmodes with $\lambda_i > 0$ and $\lambda_i < 0$, the face modes correspond to the ω^- or concave-cavity branch, while the corner modes belong to the ω^+ or convex branch. For modes tending toward $\lambda_i = 0$, the surface mode $\varepsilon = -1$ is recovered, and these modes may be said to have "edge" character.

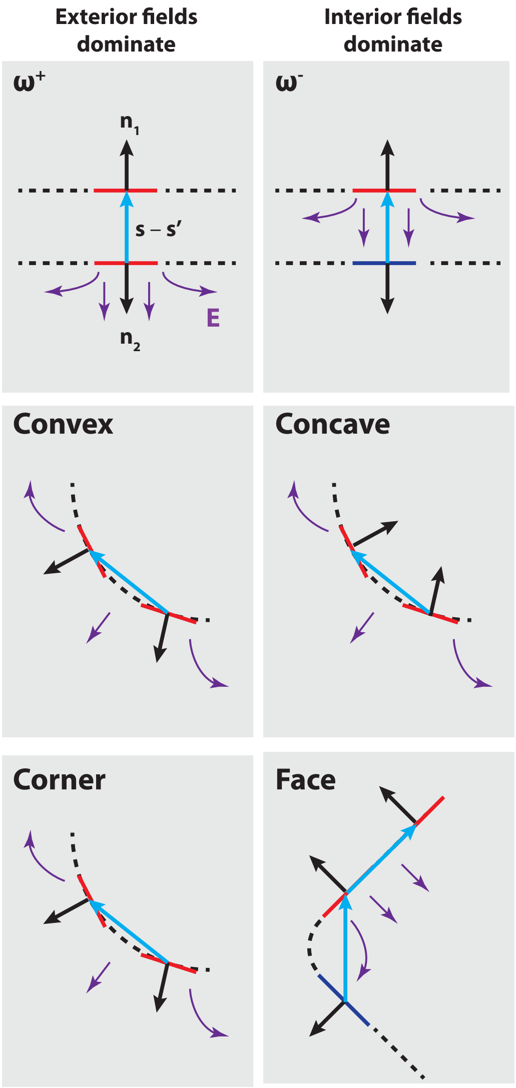

FIG. 2. Schematic illustration of key cases encountered in determining the energy of surface plasmon modes. Red and blue segments represent surface elements of opposite charge. Purple curved arrows illustrate the dominant fields. Straight arrows indicate the surface normals $\mathbf{n}$ and the separation vector $(\mathbf{s}-\mathbf{s}')$ in Eq. (7).

The origin of these two branches of shape-dependent modes can be examined further in terms of the contributions to the mode energy [Eqs. (5) and (6)] of pairs of surface elements for key geometries. Figure 2 presents a visualization of these cases. The denominator in Eq. (7) determines that contributions to the integral in Eq. (6) will be dominated by nearby surface charges of any substantial magnitude.

For a thin film the relevant surface elements will be adjacent elements as well as elements on the parallel surface. In the case of surface charges on adjacent elements, the dot product of the surface normal $\mathbf{n}$ and $(\mathbf{s}-\mathbf{s}')$ is zero. In the case of the parallel surface, $\mathbf{n}$ and $(\mathbf{s}-\mathbf{s}')$ are aligned and contribute maximally. For symmetric charges, the integral grows more negative due to the sign on F, resulting in a lowering of the mode energy (for negative ε increasing with ω). For antisymmetric charges, the contributions from the top and bottom surfaces cancel due to the change in the sign of σ. The energy splitting can also be understood in terms of the electric fields associated with the surface charges, with increased fields within the metal film for the antisymmetric charge distribution.

For a convex curved geometry, such as a sphere, the surface normals for the adjacent surface charges are no longer perpendicular to $(\mathbf{s}-\mathbf{s}')$, and the exterior fields are enhanced, resulting in similar lowering of the mode energy. For concave cavities, the fields are now in the dielectric material, resulting in an increase in mode energy. For a corner-type eigenmode, the majority of all surface elements are near zero charge, and these do not contribute to the integral. Again, nearby surface elements will have like charge and contribute to lowering the energy of the eigenmode. In contrast to corner modes, for face modes the majority of surface elements contain charge. However, for prismatic particles with flat surfaces, the charges on the same face do not contribute to the integral in Eq. (6) due to perpendicular $\mathbf{n}$ and $(\mathbf{s}-\mathbf{s}')$. The nearest contributing surface charges now appear on adjacent faces, and these are necessarily opposite in sign if charge neutrality and the characteristic symmetry of the particle surface are to be maintained. Although these "antisymmetric" charges are not on parallel surfaces as in the thin film, they contribute in the same way to the integral in Eq. (6) in that pairs of surface elements will cancel contributions to the integral due to opposite signs of the surface charges σ. As for concave cavities, the fields associated with face modes are also enhanced within the particle body, resulting in an increased energy relative to ω_S.

Langbein noted that these modes in cubic particles are bulklike due to their field distribution [26]. However, experimental EELS on surface plasmons in cubes [13] demonstrates that the modes extend into vacuum and remain part of the surface mode family. The bulklike properties noted by Langbein [26] are the preponderance of fields within the particle, and this property is reflected in the mode energies. Recent experimental evidence, as well as alternative particle geometries capitalizing on face mode coupling (Sec. III), encourages further exploration of their properties.

B. Eigenmodes of cubes and cuboctahedra

The behavior of face modes given in Sec. II A can be applied to understand trends in the eigenmodes of the continuous transition from a cube to a cuboctahedron. Throughout this transition, octahedral symmetry is maintained. Figure 3 presents the eigenmodes expressed in terms of the mode-specific dielectric function value ε_i. These modes were calculated using MNPBEM, a MATLAB (Mathworks) toolbox implementation of the BEM method [33,35]. Particle shapes were first determined using a Wulff construction MATLAB toolbox [36], and the surfaces were smoothed and meshed with level-of-detail meshing routines in AVIZO (Thermo Fisher Scientific) software. Particle surfaces were constructed of 6000 surface elements in each case, giving rise to a total of 6000 eigenmodes for each particle geometry. All 6000 eigenmodes were calculated in order to capture the face modes which are not found with solvers that calculate only a subset of the n lowest eigenmodes. The 6000-surface-element particle calculations agree for the cube geometry with values for ε_i reported by Langbein [26]. The first 6000 modes of a sphere are shown for reference as well, calculated by Eq. (4). The modes above ε_S are shown in magenta to distinguish them from the modes below ε_S, and the highest-energy modes for each octahedral-symmetric geometry are shown for reference.

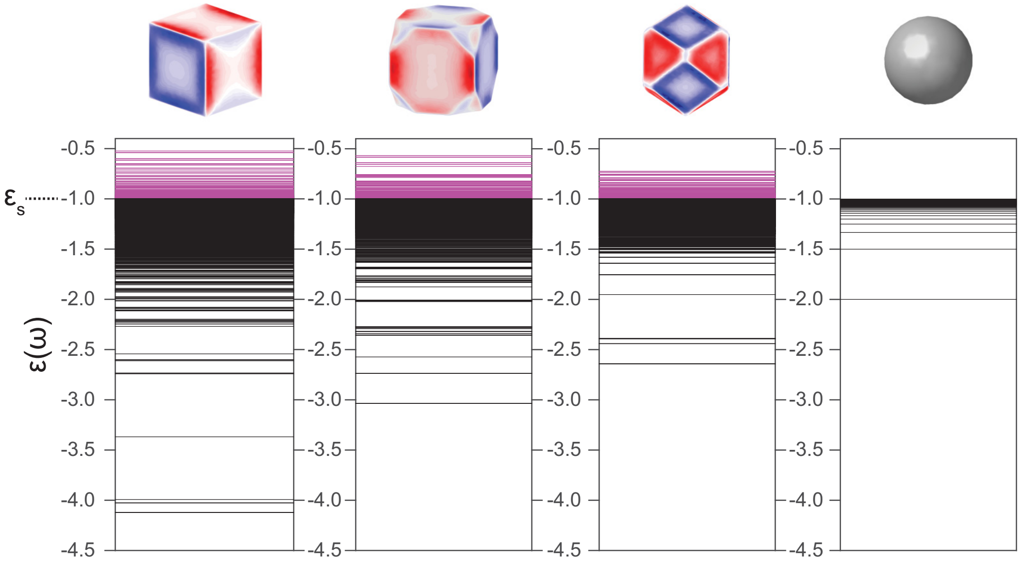

FIG. 3. Eigenmode energies [in terms of $\varepsilon(\omega)$] for a cube, a truncated cube, a cuboctahedron, and a sphere. The modes are shaded according to their position relative to the surface mode ε_S. Modes above ε_S are magenta, and modes below ε_S are black. The highest-energy mode is depicted above for the octahedral-symmetric particles.

For the cube geometry, the lowest-energy modes appear at approximately $\varepsilon = -4$, and the highest-energy modes appear at approximately $\varepsilon = -0.5$. As the cube is truncated and then transformed to a cuboctahedral geometry, the lowest-energy modes increase, and the highest-energy modes decrease. Broadly, this trend can be understood as the particle becoming more spherelike. The sphere has a lowest-energy mode at $\varepsilon = -2$, and as the faces on the cuboctahedron become more equally sized, the overall geometry transitions toward the sphere mode structure. The decrease in the highest-energy modes likewise follows as the face modes disappear for the sphere structure.

The highest-energy modes also highlight characteristics of face modes shown schematically in Fig. 2. The highest surface charge densities appear at the junctions between two perpendicular faces, as expected from Eq. (7). In all cases, the highest-energy modes (most positive ε_i) have alternating signs of the surface charge on each face, further reinforcing the relationship between the distribution of surface charges characteristic of face modes and the ω^--like behavior of the eigenmode energy.

III. FACE MODE COUPLING

The development of face modes in Sec. II establishes several hypotheses about the way in which face modes are expected to couple with other modes. For face modes to couple with corner modes, they will necessarily involve faces of a concave cavity which are expected to disperse toward more negative values of ε_i. A model system to demonstrate these predictions consists of a cubic particle containing an octahedral cavity. In this way, the symmetry of the entire particle remains octahedral, and the faces of the cavity are optimally oriented to be close and of the same symmetry character as the corners of the cube. In this geometry, the external cube face modes in turn are expected to couple with the corner modes of the cavity.

A. Modes of a cube with an octahedral cavity

Figure 4 presents the eigenmodes calculated for a cube containing an octahedral cavity, where the extent of the octahedral cavity is approximately the side length of the cube. This geometry is defined as having a relative cavity size of 1. Figure 4 shows the surface charges on the exterior as well as for the interior of the particle, where half of the particle has been removed from view. At high energy ($\varepsilon_i \approx 0$), the surface charge on the exterior is located on the cube faces, as expected. It is entirely of a single sign. This can be interpreted in the context of the interior charges, and these are shown to be entirely the opposite sign, with maximum charges at the cavity corners. The next two high-energy modes likewise show this type of antisymmetric face-corner coupling, as expected from Sec. II. Symmetry considerations for eigenmodes of nanoparticles in general define one mode as transforming like the identity (1). This is shown on the far right of Fig. 4, with a single sign of charges only on the exterior of the particle. Although this particle eigenmode does not appear in spectra of ionic crystals or plasmonic nanoparticles [its values of $\lambda_i = -2\pi$ and $\gamma_i = 1$ result in a zero in the denominator of Eq. (9)], it is present in the eigenmode description for all particles. In the cube containing an octahedral cavity, the highest-energy mode appears as the antisymmetric mode of the same underlying symmetry. In this case, the antisymmetric mode maintains the overall charge neutrality of the surface and may contribute to the photonic states of the system.

The lowest-energy corner modes exhibit the expected exterior charge distributions of the dipole (x,y,z) and quadrupole (xy,yz,xz) modes of a cube. Notably, the values of ε_i, however, are significantly shifted to lower energies than for a cube without a cavity. By examining the interior surface charges, it becomes clear that symmetric coupling with the interior octahedral faces is present in the system, as predicted given symmetry and dispersion considerations. The low-order antisymmetric modes ($\varepsilon = -0.128$ and $\varepsilon = -0.145$) present the antisymmetric pairs for dipolar and quadrupolar symmetries. These eigenmodes corroborate the explanation of face mode dispersion in Sec. II.

To establish the coupling phenomena present in this system further, a series of particles with increasing cavity sizes was simulated, as coupling depends on relative spatial proximity. Figure 5 presents the mode evolution for a cube with no cavity to a cubic frame where the "cavity" exceeds the size of the cube. Such particle geometries resemble experimentally realized hollow-frame particles [28,29]. In Fig. 5(a), the eigenmode

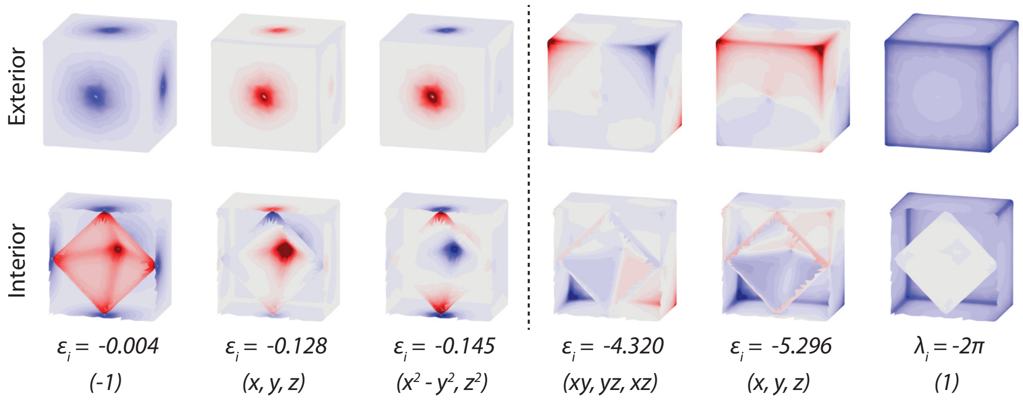

FIG. 4. Eigenmodes of a cube containing an octahedral cavity. The three highest-energy modes are shown on the left, and the three lowest-energy modes are shown on the right. The corresponding value of ε is given where defined, and the symmetry character is identified below the exterior and interior visualizations for each mode.

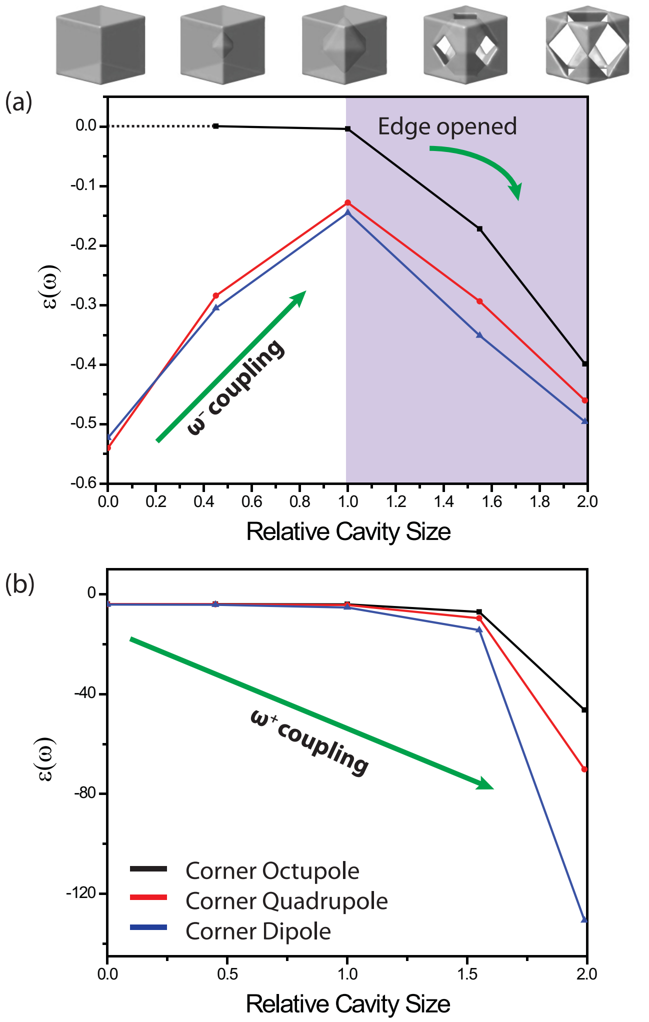

FIG. 5. (a) High-energy-branch eigenmode energies and (b) low-energy-branch eigenmode energies for increasing cavity size for a cube containing an octahedral cavity. The particle geometries are shown for reference at the top.

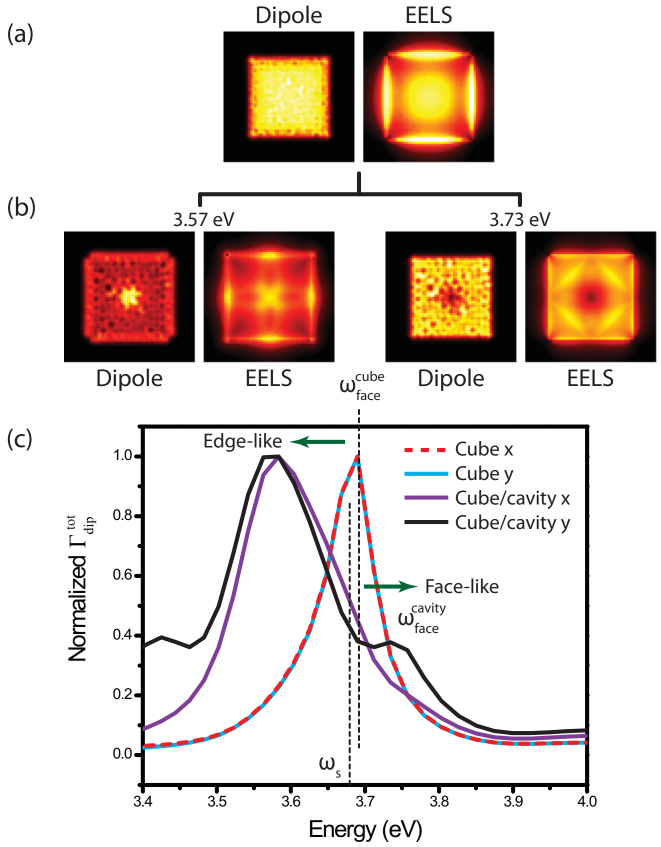

FIG. 6. (a) Maps of the position-dependent total dipole decay rate (left) and the EELS probability (right) for a cube particle at 3.7 eV. The dipole decay rate is calculated for the out-of-plane dipole orientation (x) at a plane approximately 2 nm above the particle surface. (b) Dipole decay rate x and EELS maps at 3.57 and 3.73 eV for a cube containing an octahedral cavity. (c) Dipole decay rate spectra for the out-of-plane orientation (x) and one in-plane orientation (y). Intensities in maps and the spectra are normalized from 0 to 1 for ease of comparison.

energies of the high-energy branch initially shift toward $\varepsilon = 0$ with increasing cavity size. However, when the cavity size exceeds the size of the cube, the surface area of the faces is reduced, and a new edge is opened in the structure, resulting in a decrease in the antisymmetric modes due to the increased similarity to the edge modes and the surface mode ($\varepsilon_S = -1$). In Fig. 5(b), the low-energy branch modes shift nonlinearly toward increasingly negative values of ε.

These shifts in the mode energies with cavity size reinforce the face-corner coupling suggested in Fig. 4. The ω^--like coupling of the high-energy branch modes resembles shifts toward increasingly "antibonding" states, to adopt terminology from hybridization theory [37], consistent with self-hybridization of coupled modes in the particle geometry [24]. These results also suggest an additional effect on the photonic states and spectra of these particles for both ionic crystals where the dielectric function is bounded by transverse-optical (TO) and LO phonon modes and surface plasmons where the dielectric function is bounded by 0 and ω_P. In both cases, for highly nonlinear shifts of symmetric modes toward lower energy, the corner modes will be pinned at the TO phonon mode energy ω_{TO} or near zero for surface plasmons. The upward shift of the antisymmetric modes will likewise be pinned at ω_{LO} or ω_P. This conclusion has significant implications, particularly for spatially resolved spectroscopies, such as EELS, for imaging surface phonon and surface plasmon modes. For EELS of ionic crystals, the importance of particle modes between ω_{TO} and ω_S was recently reported [8] and explained [19]. This discussion of face modes underscores the additional complexity of states between ω_S and ω_{LO} also present in these systems. For plasmonic studies, such as those for nanoframes [29], these findings provide an interpretative framework for modes and mode-coupling effects involving the high-energy branch of particle eigenmodes.

B. Optical effects of antisymmetric and cavity coupling

Although face modes have been routinely observed in convex prismatic particles, it is not obvious from eigenmode calculations alone that the mode-coupling effects in a cube containing an octahedral cavity are experimentally significant. In order to probe the effects on the observable photonic states of the system, spatially resolved dipole decay rate [38] maps and EELS maps were calculated for the cube and for the cube containing an octahedral cavity with a relative cavity size of 1. Figure 6 presents maps and dipole decay rate spectra for these particles. The total dipole decay rate is plotted as these modes are only weakly radiative. The calculations were performed in MNPBEM using the dielectric function for silver tabulated by Johnson and Christy [39].

For a convex cube particle, the conventional face mode map is recovered for both dipole decay rate and EELS (Fig. 6). However, with the addition of the cavity (see also Fig. 4), the dipole decay rate changes significantly across the face. At 3.57 eV (in the low-energy branch below ω_S), a peak appears corresponding to a map with a spike in dipole decay rate at the center of the particle face. This is corroborated in the EELS map showing EELS intensity at each of the five separable face centers (the sixth is overlapping in projection). At 3.73 eV (very close to ω_P), the identical location at the face center is significantly depleted for the dipole decay rate as well as for the EELS map. Inspection of the induced surface charges confirms that at 3.73 eV the off-center trajectories excite antisymmetric face modes with charges at the corners of the octahedral cavity.

These map features are further illustrated in the dipole decay spectra, a measure of the orientation-specific photonic states of the system [40]. In the dipole decay spectra, particularly in the in-plane y direction, a splitting of photonic states around ω_S and the nearly coincident cube face mode energy is observed. These results illustrate that the mode coupling accounted for in Fig. 4 is manifest in experimentally observable spatial and spectral signatures as a peak splitting and spatially localized rearrangement of the photonic states of the system. A Fano-like dip at the cube face mode energy in the dipole decay spectra as well as in the creation and depletion of localized states at the face center suggests unconsidered optical effects made possible through face-corner coupling in this particle/cavity geometry.

IV. SUMMARY

A framework for the interpretation of face mode dispersion in ionic crystal and plasmonic metal nanoparticles has been presented. The two fundamental branches of surface modes have been explained to link antisymmetric, concave, and face-dominated surface modes. This identification of common dispersion characteristics led to the design of a particle system with coupled face and corner modes in symmetric and antisymmetric symmetries. The consequences for the photonic states of the coupled system outline the experimental feasibility of detecting these properties with high-resolution EELS and establish principles for manipulating the optical properties of hollow-frame particles and pore structures of emerging technological interest.

ACKNOWLEDGMENT

S.M.C. acknowledges support from the Henslow Research Fellowship at Girton College, Cambridge.

---

[1] C. F. Bohren and D. R. Huffman, *Absorption and Scattering of Light by Small Particles* (Wiley, New York, 1983).

[2] F. J. García de Abajo, Phys. Rev. B **59**, 3095 (1999).

[3] S. M. Collins and P. A. Midgley, Phys. Rev. B **87**, 235432 (2013).

[4] F. J. García de Abajo and A. Howie, Phys. Rev. B **65**, 115418 (2002).

[5] A. Rivacoba, N. Zabala, and J. Aizpurua, Prog. Surf. Sci. **65**, 1 (2000).

[6] G. Boudarham and M. Kociak, Phys. Rev. B **85**, 245447 (2012).

[7] J. Nelayah, M. Kociak, O. Stéphan, F. J. García de Abajo, M. Tencé, L. Henrard, D. Taverna, I. Pastoriza-Santos, L. M. Liz-Marzán, and C. Colliex, Nat. Phys. **3**, 348 (2007).

[8] M. J. Lagos, A. Trügler, U. Hohenester, and P. E. Batson, Nature (London) **543**, 529 (2017).

[9] N. Yamamoto, K. Araya, and F. J. García de Abajo, Phys. Rev. B **64**, 205419 (2001).

[10] A. Losquin, L. F. Zagonel, V. Myroshnychenko, B. Rodríguez-González, M. Tencé, L. Scarabelli, J. Förstner, L. M. Liz-Marzán, F. J. García de Abajo, O. Stéphan, and M. Kociak, Nano Lett. **15**, 1229 (2015).

[11] K. Imaeda, S. Hasegawa, and K. Imura, J. Phys. Chem. C **122**, 7399 (2018).

[12] S. Mazzucco, N. Geuquet, J. Ye, O. Stéphan, W. Van Roy, P. Van Dorpe, L. Henrard, and M. Kociak, Nano Lett. **12**, 1288 (2012).

[13] O. Nicoletti, F. de la Peña, R. K. Leary, D. J. Holland, C. Ducati, and P. A. Midgley, Nature (London) **502**, 80 (2013).

[14] S. M. Collins, E. Ringe, M. Duchamp, Z. Saghi, R. E. Dunin-Borkowski, and P. A. Midgley, ACS Photonics **2**, 1628 (2015).

[15] V. Myroshnychenko, J. Nelayah, G. Adamo, N. Geuquet, J. Rodríguez-Fernández, I. Pastoriza-Santos, K. F. MacDonald, L. Henrard, L. M. Liz-Marzán, N. I. Zheludev, M. Kociak, and F. J. García de Abajo, Nano Lett. **12**, 4172 (2012).

[16] D. Rossouw, M. Couillard, J. Vickery, E. Kumacheva, and G. A. Botton, Nano Lett. **11**, 1499 (2011).

[17] O. Nicoletti, M. Wubs, N. A. Mortensen, W. Sigle, P. A. van Aken, and P. A. Midgley, Opt. Express **19**, 15371 (2011).

[18] D. Rossouw and G. A. Botton, Phys. Rev. Lett. **110**, 066801 (2013).

[19] H. Lourenço-Martins and M. Kociak, Phys. Rev. X **7**, 041059 (2017).

[20] F.-P. Schmidt, H. Ditlbacher, U. Hohenester, A. Hohenau, F. Hofer, and J. R. Krenn, Nat. Commun. **5**, 3604 (2014).

[21] A. Hörl, A. Trügler, and U. Hohenester, Phys. Rev. Lett. **111**, 076801 (2013).

[22] A. Hörl, A. Trügler, and U. Hohenester, ACS Photonics **2**, 1429 (2015).

[23] G. Haberfehlner, A. Trügler, F. P. Schmidt, A. Hörl, F. Hofer, U. Hohenester, and G. Kothleitner, Nano Lett. **15**, 7726 (2015).

[24] H. Lourenço-Martins, P. Das, L. H. G. Tizei, R. Weil, and M. Kociak, Nat. Phys. **14**, 360 (2018).

[25] R. Fuchs, Phys. Rev. B **11**, 1732 (1975).
[26] D. Langbein, J. Phys. A **9**, 627 (1976).
[27] Y. Zhu, P. N. H. Nakashima, A. M. Funston, L. Bourgeois, and J. Etheridge, ACS Nano **11**, 11383 (2017).
[28] E. González, J. Arbiol, and V. F. Puntes, Science **334**, 1377 (2011).
[29] A. Genç, J. Patarroyo, J. Sancho-Parramon, R. Arenal, M. Duchamp, E. E. Gonzalez, L. Henrard, N. G. Bastús, R. E. Dunin-Borkowski, V. F. Puntes, and J. Arbiol, ACS Photonics **3**, 770 (2016).
[30] S. P. Apell, P. M. Echenique, and R. H. Ritchie, Ultramicroscopy **65**, 53 (1996).
[31] C. R. Crick, P. Albella, H.-J. Kim, A. P. Ivanov, K.-B. Kim, S. A. Maier, and J. B. Edel, ACS Photonics **4**, 2835 (2017).
[32] O. N. Assad, T. Gilboa, J. Spitzberg, M. Juhasz, E. Weinhold, and A. Meller, Adv. Mater. **29**, 1605442 (2017).
[33] U. Hohenester and A. Trügler, Comput. Phys. Commun. **183**, 370 (2012).
[34] M. Kociak and O. Stéphan, Chem. Soc. Rev. **43**, 3865 (2014).
[35] U. Hohenester, Comput. Phys. Commun. **185**, 1177 (2014).
[36] E. Ringe, R. P. Van Duyne, and L. D. Marks, J. Phys. Chem. C **117**, 15859 (2013).
[37] E. Prodan, C. Radloff, N. J. Halas, and P. Nordlander, Science **302**, 419 (2003).
[38] U. Hohenester and A. Trügler, IEEE J. Sel. Top. Quantum Electron. **14**, 1430 (2008).
[39] P. B. Johnson and R. W. Christy, Phys. Rev. B **6**, 4370 (1972).
[40] U. Hohenester, H. Ditlbacher, and J. R. Krenn, Phys. Rev. Lett. **103**, 106801 (2009).